



Understanding water reaction pathways to control the hydrolytic reactivity of a Zn metal-organic framework

Received: 8 April 2024

Accepted: 8 November 2024

Published online: 30 December 2024

Check for updates

Shoushun Chen^{1,8}✉, Zelin Zhang^{2,8}, Wei Chen^{3,8}, Bryan E. G. Lucier⁴,
Mansheng Chen^{4,5}, Wanli Zhang⁴, Haihong Zhu¹, Ivan Hung⁶,
Anmin Zheng^{3,7}, Zhehong Gan⁶, Dongsheng Lei²✉ & Yining Huang⁴✉

Metal-organic frameworks (MOFs) are a class of porous materials that are of topical interest for their utility in water-related applications. Nevertheless, molecular-level insight into water-MOF interactions and MOF hydrolytic reactivity remains understudied. Herein, we report two hydrolytic pathways leading to either structural stability or framework decomposition of a MOF (ZnMOF-1). The two distinct ZnMOF-1 water reaction pathways are linked to the diffusion rate of incorporated guest dimethylformamide (DMF) molecules: slow diffusion of DMF triggers evolution of the initial MOF into a water-stable MOF product exhibiting enhanced water adsorption, while fast exchange of DMF with water leads to decomposition. The starting MOF, three intermediates from the water reaction pathways and the final stable MOF have been characterized. The documentation of two distinct pathways counters the stereotype that water exposure always leads to destruction or degradation of water-sensitive MOFs, and demonstrates that water-stable MOFs with improved adsorption properties can be prepared via controlled solvent-triggered structural rearrangement.

MOFs are a class of porous materials constructed of inorganic nodes joined by organic linkers^{1–3}. The diversity of potential MOF structures and pore motifs makes these materials promising candidates in applications from gas adsorption/separation^{4,5} to chemical sensing^{6,7} and catalysis^{8–10}. The many possible MOF pore sizes and shapes permit accommodation of guest molecules that can play a role in the eventual material properties. Obtaining a deeper understanding of host-guest interactions in MOFs is thus critical for insight into structure-property relationships including hydrolytic stability^{11–13}. Water is ubiquitous in

nature, and the moisture sensitivity of many early-generation MOFs was considered a hindrance to practical applications^{14,15}. Rational MOF design strategies, including the incorporation of high valence metals like Zr⁴⁺ and Al³⁺ with carboxylic acid linkers^{16,17}, or using divalent soft metals such as Ni²⁺ and Zn²⁺ with soft base azolate ligands^{18,19}, have produced many MOFs with excellent hydrolytic stability. The number of water-stable MOFs reported with potential practical applications^{20–22}, including those based on water adsorption, such as water harvesting and refrigeration^{23–26}, is continually growing.

¹Lanzhou Magnetic Resonance Center, Frontiers Science Center for Rare Isotopes, College of Chemistry and Chemical Engineering, Lanzhou University, Lanzhou 730000, China. ²School of Physical Science and Technology, Electron Microscopy Centre of Lanzhou University, Lanzhou University, Lanzhou 730000, China. ³Innovation Academy for Precision Measurement Science and Technology, Chinese Academy of Sciences, Wuhan 430071, China.

⁴Department of Chemistry, University of Western Ontario, London, Ontario N6A 5B7, Canada. ⁵Key Laboratory of Functional Organometallic Materials, College of Chemistry and Materials Science, Hengyang Normal University, Hengyang, Hunan 421008, China. ⁶National High Magnetic Field Laboratory (NHMFL), 1800 East Paul Dirac Dr, Tallahassee, Florida 32310, USA. ⁷Interdisciplinary Institute of NMR and Molecular Sciences, Hubei Province for Coal Conversion and New Carbon Materials, School of Chemistry and Chemical Engineering, Wuhan University of Science and Technology, Wuhan 430081, China. ⁸These authors contributed equally: Shoushun Chen, Zelin Zhang, Wei Chen. ✉e-mail: chenss@lzu.edu.cn; leids@lzu.edu.cn; yhuang@uwo.ca

In general, there are two broad MOF classifications with regard to water interactions: (i) water-sensitive MOFs that lose long-range order upon water exposure, leading to the collapse of the structure^{27–29}; and (ii) MOFs which have high hydrolytic stability and retain structural integrity and porosity in the presence of water^{30–32}. These two categories oversimplify the possible outcomes of water exposure, as there are tens of thousands of MOFs and virtually limitless structural possibilities. Several modern examples have redefined the role of water in MOF structures and applications. A recent study examined the $\text{Zn}_2(\text{BDC-TM})_2(\text{DABCO})$ MOF, which exhibits high water stability but also features a water-induced structural defect that is reversible following water desorption³³, exemplifying how the relationship between water and water-stable MOFs is more nuanced than previously thought. Water can also have a strong influence on MOF guest adsorption. Confined water in a Cu MOF has been shown to unlock exclusive adsorption of C_3H_6 over C_3H_8 ³⁴, and adsorbed water greatly assists diffusion of the nerve agent simulant dimethyl methyl phosphonate (DMMP) in a Zr-based MOF rather than simply blocking the pores³⁵, which are both unexpected findings that challenge commonly-held beliefs in the field.

Herein, we report the existence of two distinct structural transformation pathways in a Zn-based MOF, Zn(BTEC)(Trz) (termed ZnMOF-1, BTEC: benzene-1,2,4,5-tetracarboxylic acid, Trz: 1,2,4-triazole)³⁶, upon immersion in water. The bulk of the water-sensitive ZnMOF-1 proceeds along a route with multiple single crystal to single crystal (SCSC) structural rearrangements that eventually yields a water-stable porous three-dimensional (3D) Zn MOF; two intermediates and the final product have been isolated and structurally characterized by single crystal X-ray diffraction (SCXRD). In contrast, a small amount of ZnMOF-1 follows the second reaction pathway, which ends with structural collapse and dissolution of MOF constituents in the water medium. A key transient intermediate in this destructive

pathway has also been isolated and identified by advanced cryogenic electron microscopy (cryo-EM) and microcrystal electron diffraction (microED) techniques. Multinuclear solid-state nuclear magnetic resonance (SSNMR) spectroscopy reveals that encapsulated DMF within the original ZnMOF-1 structure plays a critical role in both structural transformation routes. This work demonstrates that water does not always lead to the destruction or degradation of water-sensitive MOFs, and provides insight into why this is.

Results

Effects of water immersion on MOF porosity and guest adsorption

ZnMOF-1 incorporates both BTEC and Trz ligands in a mixed-linker configuration (Fig. 1a). ZnMOF-1 features a 3D structure (Fig. 1b) and is classified as a pillared layered metal-organic framework³⁷. The samples in this work are termed ZnMOF-1-*xxs*/min/h/day, where *xxs*/min/h/day denotes the duration of water exposure (e.g., ZnMOF-1-15min is as-made ZnMOF-1 after 15 min); please see the SI for experimental details.

ZnMOF-1 has a CO_2 adsorption capacity of $47.3 \text{ cm}^3/\text{g}$ and remains crystalline after exposure to a high-humidity environment for at least eight days (Fig. 1c, d). The CO_2 adsorption capacity increases a little at first but quickly becomes practically non-porous to CO_2 ($< 5 \text{ cm}^3/\text{g}$, Fig. 1d). In contrast, the water adsorption capacity of ZnMOF-1-48h is enhanced from $150.0 \text{ cm}^3/\text{g}$ to $228.9 \text{ cm}^3/\text{g}$ (Fig. 1e). While ZnMOF-4 has a superior water sorption capacity versus that of ZnMOF-1, the overall magnitude of water sorption in both systems remains limited. ZnMOF-1-48h appears to be more porous than ZnMOF-1, which runs contrary to the significant porosity loss that would be expected from the water-sensitive ZnMOF-1. The adsorption data of ZnMOF-1-48h suggests that its structure is accessible to water but not CO_2 . The kinetic diameters of CO_2 and H_2O are 3.3 \AA ^{38,39} and 2.6 \AA ⁴⁰, respectively. This implies that ZnMOF-1-48h should have a pore diameter on the

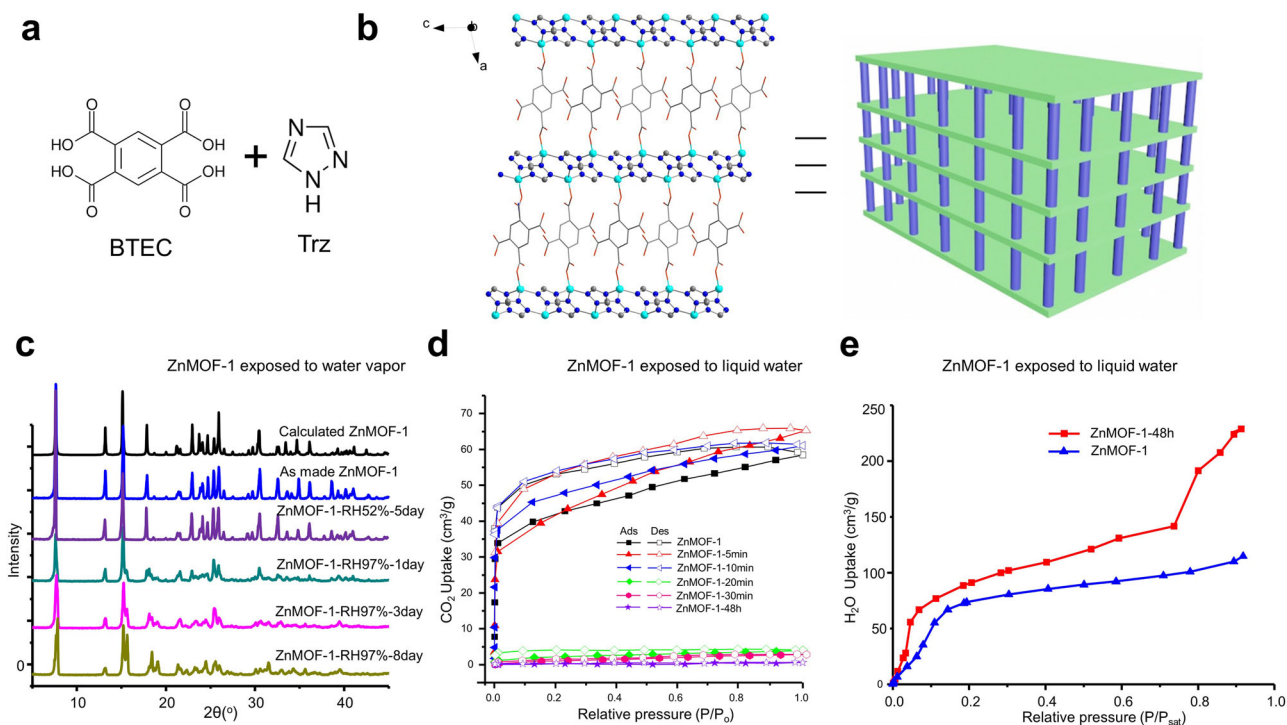


Fig. 1 | Structure and gas sorption data of ZnMOF-1. **a** The BTEC and Trz ligands incorporated within ZnMOF-1. **b** An illustration of the 3D pillared layered structure of ZnMOF-1. Carbon is gray, oxygen is red, nitrogen is dark blue, and zinc is light blue. **c** The PXRD patterns of ZnMOF-1 under high humidity environments are shown. The RH (relative humidity) was created by saturated aqueous salts

$\text{Mg}(\text{NO}_3)_2$ (RH: 52%) and K_2SO_4 (RH: 97%). **d** The CO_2 sorption isotherms for ZnMOF-1 samples (195 K, 1 bar). **e** The water sorption isotherms for ZnMOF-1 samples, as obtained at 298 K. The P_{sat} term refers to the saturation water vapor pressure. All samples in **d** and **e** were immersed in liquid water prior to analysis, with the immersion time indicated in the corresponding label.

order of ca. 3 Å. A comparison of ZnMOF-1-48h and original ZnMOF-1 revealed that a significant loss of solid occurred during the time ZnMOF-1 was exposed to water. To more quantitatively determine the mass loss, the filtrate of ZnMOF-1-48h was subjected to ICP-OES (inductively coupled plasma-optical emission spectrometry). It was found that 17.15 % of Zn from the initial ZnMOF-1 sample had dissolved while stirring (Supplementary Table 1). In addition, the filtrate of ZnMOF-1 samples obtained after specific durations of water exposure were collected and examined via ^1H solution NMR. Characteristic ^1H resonances from the BTEC and Trz ligands, along with the DMF solvent, were all apparent (Supplementary Figs. 1–5). Taken together, the sorption isotherms, ICP-OES, and solution NMR data indicate that there is some alternate reaction that occurs separate from the ZnMOF-1 to ZnMOF-1-48h conversion pathway.

ZnMOF single-crystal to single-crystal transitions

ZnMOF-1 single crystals undergo a rare SCSC transition in water which can be exploited to conclusively identify and characterize the intermediate states of ZnMOF-2 and ZnMOF-3, along with the final water stable phase termed ZnMOF-4. The SCSC transition was found to occur when single crystals of ZnMOF-1 were submerged in water held at a set temperature of 25 °C without any agitation. All single crystals of ZnMOF-2, -3, and -4 were harvested at different times from the same initial batch of ZnMOF-1 single crystals immersed in water. We found that it required at least 1 h to obtain ZnMOF-2 single crystals of sufficient quality for analysis, it took 2 h to obtain single crystals of ZnMOF-3, and about 24 h was needed to isolate suitable single crystals of ZnMOF-4. ZnMOF-1 crystallizes in the monoclinic space group $P2_1/c$. As-made ZnMOF-1 incorporates two guest DMF molecules ($[\text{Zn}_2(\text{H}_2\text{BTEC})(\text{Trz})_2]\cdot 2\text{DMF}$) and there is one unique Zn site (Fig. 2a). The 3D structure of porous ZnMOF-1 consists of 2D sheets of Zn ions and bridging Trz linkers (Fig. 2a-II, Supplementary Fig. 6a) which are pillared by BTEC linkers (Supplementary Fig. 6b). This arrangement gives rise to a porous three-dimensional framework with vacant pores along the a -axis measuring 8.9×7.9 Å (Fig. 2a-I). There is also a separate set of 6.7×7.8 Å pores along the c -axis (Supplementary Fig. 7)³⁶. ZnMOF-1 features unbound BTEC carboxyl groups (Fig. 2a-II, Supplementary Fig. 6b). There are three N atoms from separate Trz linkers and one oxygen atom from BTEC coordinated to Zn (Fig. 2a-III). ZnMOF-1 was reported to be stable in water³⁶; however, we found this material was stable in high humidity conditions but unstable upon exposure to liquid water. The difference in H_2O concentration between water vapor and liquid water seems to be a key factor in the hydrolytic stability of ZnMOF-1. This MOF contains tetrahedral Zn ions that are accessible to water, and it is well established that MOFs containing Zn^{2+} tetrahedrally bound to oxygen atoms of carboxylate linkers tend to collapse or decompose in water^{14,41,42}.

After immersing ZnMOF-1 in water, the first intermediate is ZnMOF-2 ($[\text{Zn}_2(\text{BTEC})_{0.75}(\text{Trz})(\text{DMF})_2]\cdot 2\text{DMF}$) (Fig. 2b), which is a 3D porous MOF that crystallizes in the monoclinic $C2/m$ space group. The 3D structure of ZnMOF-2 features two types of pores, where one system is a linear $9.9 \text{ Å} \times 6.2 \text{ Å}$ channel (Fig. 2b-I) and the other is a zig-zag $11.0 \text{ Å} \times 9.4 \text{ Å}$ pore along the c -axis (Supplementary Fig. 9b). ZnMOF-2 has a pillared layered 3D structure similar to that of ZnMOF-1, in which the BTEC linkers act as pillars to connect adjacent layers composed of two unique tetrahedral Zn ions (denoted Zn1 and Zn2) (Fig. 2b-I, II). Zn1 and Zn2 are bound to two N atoms from two Trz linkers and two oxygen atoms from two BTEC linkers (Fig. 2b-III). There is also a six-coordinate Zn site (Zn3) bound to four O atoms from equatorial BTEC linkers and two O atoms from axial DMF linkers (Fig. 2b-III, Supplementary Fig. 9c). The unit cell volume of ZnMOF-2 is 3774 Å^3 , which is much larger than the 1254 Å^3 unit cell of ZnMOF-1 (Supplementary Table 2). ZnMOF-1 undergoes structural expansion upon water immersion, as reflected by the slight increase in CO_2 capacity after 5 min of water exposure (Fig. 1d).

The BTEC carboxyl groups are all coordinated to Zn atoms in ZnMOF-2 (Fig. 2b-II). During the phase change from ZnMOF-1 to ZnMOF-2, the Zn coordination sphere is rearranged in two ways. The first rearrangement involves breaking one of the three Zn-N bonds to Trz linkers from the Zn site in ZnMOF-1 (Fig. 2b-III), which leads to a differentiation between Zn1 and Zn2 sites, where Zn2 features a newly-formed Zn-O bond from a BTEC linker (Fig. 2b-II). The second rearrangement is the cleavage of Zn-N bonds from select Zn centers, resulting in a six-coordinate Zn site (Zn3) (Fig. 2b-III). Since ZnMOF-1 is stable in high humidity (Fig. 1c), the phase change from ZnMOF-1 to ZnMOF-2 is unlikely to be directly caused by water molecules, but could instead be triggered by the increased internal dynamics of encapsulated DMF upon exposure to liquid water stimuli. The increased internal dynamics would allow DMF guests to rapidly enter and exit the Zn local environment, forming transient bonds. This phenomenon was documented in the Zn-based MOF-5, where solvent DMF can reversibly bind with tetrahedral Zn MOF-5 site, leading to Zn centers which rapidly oscillate between four- and six-coordinate geometries⁴³. To investigate further, the ZnMOF-1 synthesis temperature was deliberately adjusted from 100 to 130 °C to see if a higher synthetic temperature also triggered DMF attack of Zn centers. A mixture of ZnMOF-1 and ZnMOF-2 crystals was harvested at a temperature 130 °C (Supplementary Fig. 10) suggesting that increased temperature also results in increased DMF dynamics and the formation of ZnMOF-2. Pure powdered ZnMOF-2 was also obtained by immersing ZnMOF-1 into a 95:5 v/v mixture of DMF and water (please refer to the SI). Both findings indicate that DMF dynamics and associated Zn attack are the main mechanism of structural transformation from ZnMOF-1 to -2.

The structural evolution in this system does not stop at ZnMOF-2, leading to the emergence of ZnMOF-3 [$\text{Zn}_2(\text{BTEC})(\text{HTrz})_4$], a 1D MOF with a chain-like structure (Fig. 2c, Supplementary Fig. 11) that crystallized in the triclinic $P-1$ space group. ZnMOF-3 has one Zn site that coordinated to two N atoms (Trz) and two oxygen atoms (BTEC) in a distorted tetrahedral coordination sphere (Fig. 2c-III, Supplementary Fig. 11); however, each Trz linker in ZnMOF-3 is only bound to a single Zn center, yielding a 1D chain structure (Fig. 2c-II). There are no identifiable DMF molecules in ZnMOF-3 (Fig. 2c-I) and that release of DMF is responsible for the phase transition from ZnMOF-2 to ZnMOF-3. A lattice rearrangement triggered by removal of guest solvents in MOF systems, particularly coordinated solvents, allows the resulting coordinatively unsaturated metal centres to adjust their bonding arrangement to achieve saturation, usually resulting in a significant crystal structural change^{44–47}. While the departure of DMF from the framework initiates the structural change from ZnMOF-2 to ZnMOF-3, but other components of the frameworks in solid or dissolved forms may also play a role during the phase change. It appears that the single tetrahedral Zn in ZnMOF-1 first changes to the octahedral Zn3 site in ZnMOF-2, then back to a single tetrahedral Zn in ZnMOF-3, in a process reminiscent of the dynamic DMF binding with Zn in MOF-5⁴³. In this instance, it is apparent that water is the driving force to purge DMF from ZnMOF-2 and push structural evolution to ZnMOF-3. The largest distance between two neighboring layers in ZnMOF-3 is 8.28 Å (Fig. 2c-I), but no water molecules were found between adjacent layers, hinting that water does not enter the framework during phase changes. This hypothesis was investigated using multinuclear SSNMR (*vide infra*).

Once formed, ZnMOF-3 underwent further structural evolution in water. ZnMOF-3 transformed into a 3D MOF, ZnMOF-4 (Fig. 2d-I), which is water-stable and incorporates coordinated water molecules as evidence of water penetration within the MOF structure; ZnMOF-4 is the final product of the dominant structural rearrangement route of ZnMOF-1 in water (i.e. The ZnMOF-1-48h). ZnMOF-4 has the formula $[\text{Zn}_3(\text{BTEC})(\text{Trz})_2(\text{H}_2\text{O})_4]\cdot 2\text{H}_2\text{O}$ and crystallized in the triclinic $P-1$ space group⁴⁸ ZnMOF-4 is a 3D porous MOF with an accessible pore size of

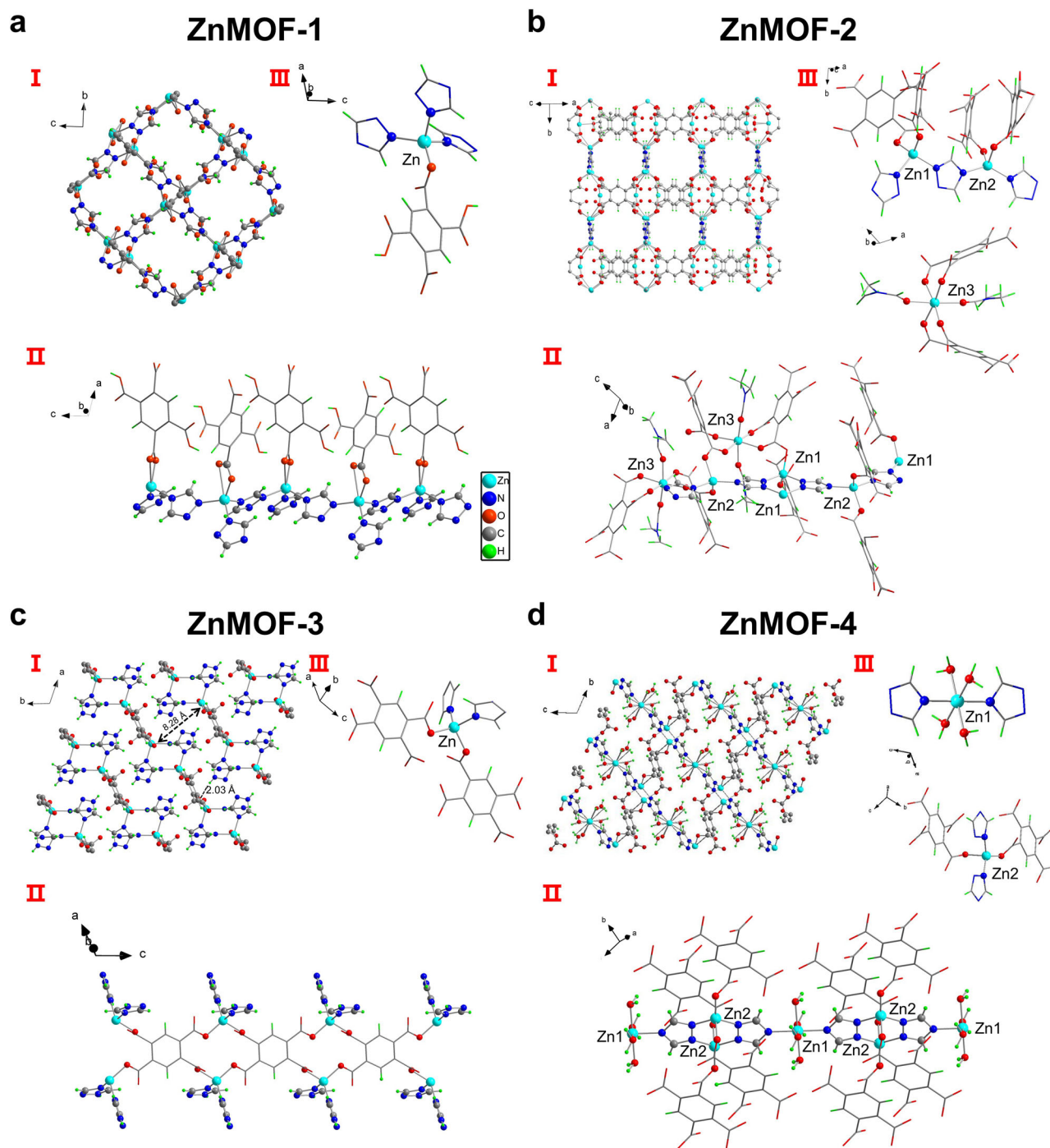


Fig. 2 | Crystal structures of ZnMOF-1/2/3/4. The structures of ZnMOF-1/2/3/4, along with their local Zn environments, are depicted in (a–d), respectively. The guest DMF in ZnMOF-1 and ZnMOF-2 are omitted for clarity.

3.1 Å along the a -axis, which agrees well with the 3 Å pore size estimated from ZnMOF-1-48h CO₂ and H₂O adsorption data (Fig. 1d, e). There are two independent Zn sites in ZnMOF-4, octahedral six-coordinate Zn1 and tetrahedral four-coordinate Zn2 (Fig. 2d-III). Zn1 is equatorially linked to four water molecules and axially bound to two nitrogen atoms from Trz linkers, but there are no bound BTEC linkers, suggesting water molecules break the bonds between Zn and BTEC linker in the transition from ZnMOF-3 (Fig. 2c-II) to ZnMOF-4; these observations confirm that four-coordinate Zn is not stable in the presence of water^{49,50} and that the Zn-O bonds are more susceptible to water attack versus Zn-N bonds. Interestingly, only one-third of tetrahedral Zn centers in ZnMOF-3 become octahedral Zn1 sites in ZnMOF-4

(Fig. 2d-II), and Zn2 sites that do not react with water (Fig. 2d-III). The linkers around the Zn2 sites in ZnMOF-4 now sterically shield the metal to prevent water attack, as shown by the space-filling model in Supplementary Fig. 12^{15,18,51}. This steric protection of Zn2 confers water stability on ZnMOF-4. The main structural transformation pathway of ZnMOF-1 in water is now clear, however, the 17.15 % Zn loss from ZnMOF-1 to ZnMOF-4 remains unexplained.

PXRD of ZnMOF-1 and water reaction products

Powdered samples of ZnMOF-1 were stirred in water for various durations and then characterized using PXRD. The PXRD diffraction patterns (Fig. 3a) verified the presence of pure as-made ZnMOF-1/2 samples,

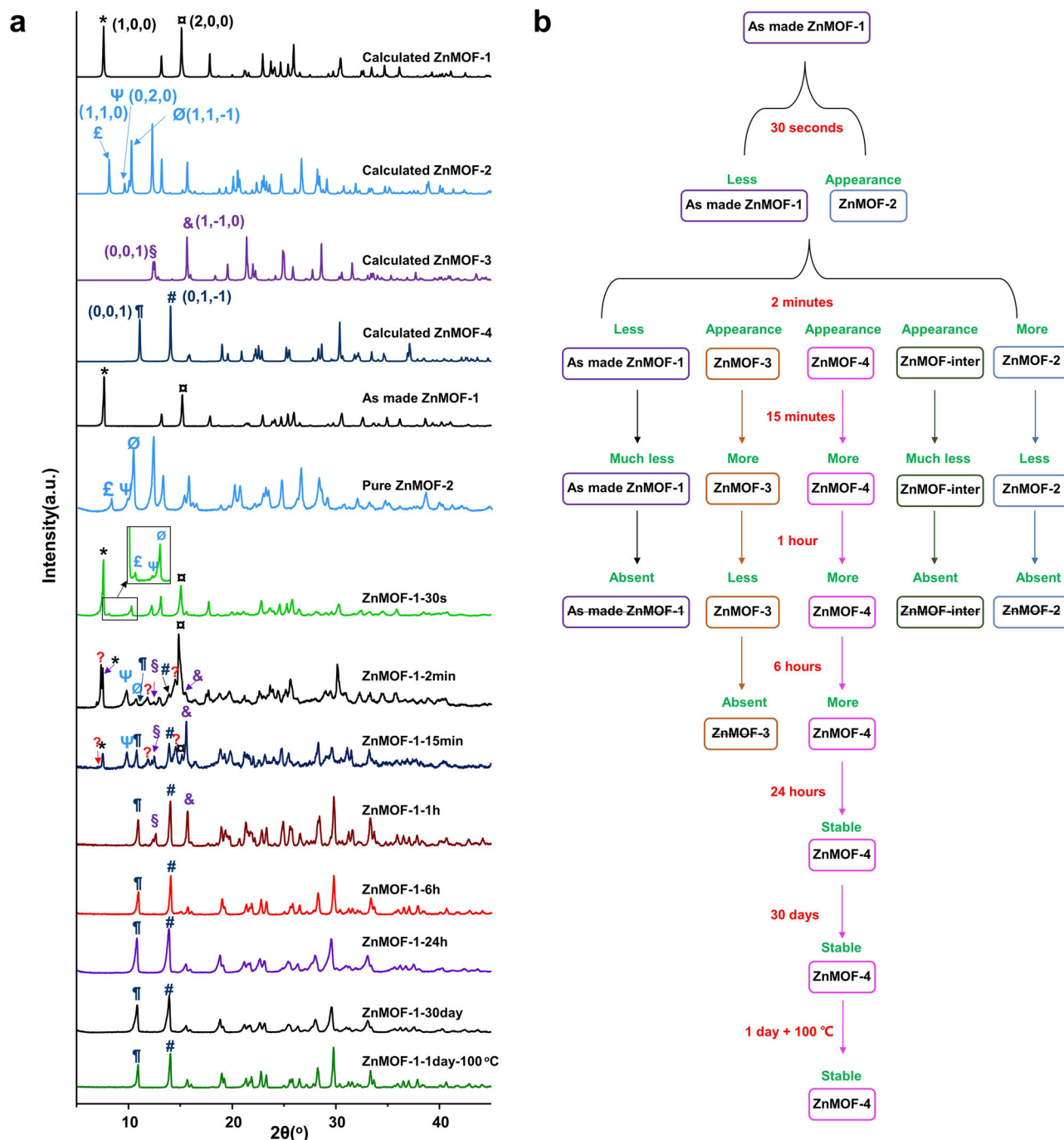


Fig. 3 | PXRD data of Zn MOFs. a The calculated PXRD patterns of ZnMOF-1/2/3/4, along with the experimental patterns of as-made ZnMOF-1, ZnMOF-2, and water-treated ZnMOF-1. The various symbols are used to mark the reflections in each MOF. The red question mark (?) signifies unassigned reflections originating from

the unknown phase termed ZnMOF-inter. **b** A flow chart outlining the structural changes observed via PXRD upon immersion of as-made ZnMOF-1 in liquid water. The absence of a specific phase means that the phase could not be observed via PXRD.

along with ZnMOF-1, -2, -3 and -4 samples after water immersion. After only 30 s of water immersion, the ZnMOF-1-30s sample yielded low-intensity reflections from ZnMOF-2 (£, Ψ and Ø in Fig. 3a), indicating the rapid onset of water-induced structural changes. The ZnMOF-1-2min diffractogram shows evidence of increased ZnMOF-2 formation, while patterns from ZnMOF-3 (reflections marked with § and &) and ZnMOF-4 (reflections indicated by ¶ and #) began to appear. The intensities of the ZnMOF-1 reflections in the ZnMOF-1-2min diffractogram, denoted by * and □, were significantly diminished as ZnMOF-1 transformed to ZnMOF-2. Surprisingly, an additional set of unassigned reflections, marked with red question marks,

also appeared. The PXRD diffractogram of ZnMOF-1-15min reveals that reflections corresponding to the unidentified phase have been significantly reduced in intensity, indicating that the unidentified phase was not stable in water. A more detailed indexed PXRD diffractogram of ZnMOF-1-2min and ZnMOF-1-15min samples can be found in Supplementary Fig. 13.

The ZnMOF-1-1h diffractogram does not feature any apparent reflections from ZnMOF-1, ZnMOF-2, or the unidentified phase, leaving ZnMOF-3 and ZnMOF-4 as the main constituents. The PXRD pattern of ZnMOF-1-6h shows that ZnMOF-3 was fully converted to ZnMOF-4 after 6 h. The structure of ZnMOF-4 was stable to long-term water

exposure and immersion in boiling water (Fig. 3a). It is worth noting that ZnMOF-4 was found to be very stable while immersed in DMF for one week at both room temperature and at 120 °C (Supplementary Fig. 14), which suggests that the structural transformation from ZnMOF-1 to ZnMOF-4 is irreversible. A flow chart depicting the entire water-induced structural transformation process as determined from PXRD data is provided in Fig. 3b. The unidentified phase denoted by red question marks could not be indexed to any of the four ZnMOF structures, signifying the existence of another intermediate phase which we have termed ZnMOF-inter. The presence of ZnMOF-inter hints that there was either an additional step in the path from ZnMOF-1 to ZnMOF-4, or a separate decomposition route accounting for the 17.72 % Zn mass loss from ZnMOF-1 to ZnMOF-4.

Cryo-EM and microED studies

In order to further investigate the structure of ZnMOF-inter, and probe any possible structural discrepancies between ZnMOF samples immersed in water versus those removed from water and dried, cryo-EM analysis was performed. Our cryo-EM experiments examined ZnMOF-1 samples frozen in a hydrated state, permitting in situ observations of the MOF structure during water-induced structural rearrangement and enabling characterization of unstable intermediate states^{52,53}. The use of cryogenic temperatures is necessary for any electron diffraction experiments on as-made ZnMOF-1 along with its intermediate states, as they are highly sensitive to electron bombardment at room temperature (Supplementary Fig. 15)^{54,55}. ZnMOF-1 crystals were frozen immediately after water immersion and subjected to cryo-EM. A majority of the crystals produced an electron diffraction pattern indicative of the ZnMOF-1 crystal structure (Fig. 4a). Crystals corresponding to ZnMOF-2 (Fig. 4b) and ZnMOF-3 materials (Fig. 4c) were found in ZnMOF-1 samples frozen after 10 min of water treatment, and crystals of ZnMOF-4 (Fig. 4d) were isolated from a sample exposed to water for 20 min.

There were some crystals that exhibited diffraction patterns distinct from ZnMOF-1, -2, -3 or -4; these particles may correspond to the ZnMOF-inter phase (Fig. 4e). The crystals have a *Pnma* space group with a unit cell of $a = 17.93 \text{ \AA}$, $b = 35.06 \text{ \AA}$, $c = 28.44 \text{ \AA}$, distinct from those of ZnMOF-1, -2, -3, and -4 (Supplementary Table 2). The calculated PXRD pattern of this MOF yielded low-angle reflections at 7.7, 11.7, and 14.0°, which are excellent matches for the unassigned reflections (red question marks, Fig. 4f) and confirm the existence of ZnMOF-inter. The structure of ZnMOF-inter was determined using microED^{56,57}. ZnMOF-inter was difficult to characterize as it was poorly crystalline and disordered. This disorder is likely an intrinsic feature of ZnMOF-inter, which appears to be a transient phase that continuously changes during hydrolysis. As a result, we were restricted to refining the structure using isotropic atomic displacement parameters, and modeling only some of the guest water molecules in the pores (Fig. 4g). ZnMOF-inter ($[\text{Zn}_{38}(\text{BTEC})_{12}(\text{Trz})_{28}(\text{H}_2\text{O})_{51}]\cdot 36\text{H}_2\text{O}$) has a 3D porous structure with pores measuring $9.9 \times 8.0 \text{ \AA}$ along the *a*-axis. There are ten unique Zn sites, which can be divided into three types: (1) tetrahedral Zn1, Zn4, Zn5, and Zn8 sites that have BTEC and Trz linkers, (2) octahedral Zn2, Zn3, Zn7, Zn9 and Zn10 sites which have two to five coordinated water molecules, and (3) octahedral Zn6 which is coordinated to all Trz linkers. The 17881 Å³ unit cell volume of ZnMOF-inter is much larger than those of ZnMOF-1, -2, -3, -4 (Supplementary Table 2); in combination with the ten various Zn sites, the difficulties in obtaining samples of sufficient crystallinity and the rapid reduction in corresponding PXRD reflection intensities during stirring (Fig. 4f), it appears that ZnMOF-inter is an unstable transition phase. The Zn mass loss observed from ICP-OES suggests there is a dissolution pathway, and the unstable ZnMOF-inter appears to be a key point along this route.

The unusual structure of ZnMOF-inter is also an opportunity to peer deeper into this MOF water decomposition mechanism. The

current knowledge of MOF water decomposition pathways largely relies on theoretical calculations, due to the difficulties in obtaining accurate intermediate state^{49,50,58,59}. The structure of ZnMOF-inter indicates that water decomposition of MOFs is able to proceed along an avenue where water molecules progressively coordinate with an increasing number of metal centers, eventually reaching a specific saturation level of water-metal coordination that results in structural collapse of the MOF. ZnMOF-inter appears to arise as a product of rapid exchange between guest DMF and water, which is only possible on the surface of ZnMOF-1 crystals or within small crystallites. As ZnMOF-inter is a key solid form along the MOF decomposition pathway, the amount of ZnMOF-inter formed is indirectly indicated by the dissolved Zn mass loss. The Zn mass loss was found to be 15.33 wt % when a sample of single crystals was immersed in water without stirring, and the Zn loss was largely increased by about 23.4% and reached a value of 18.91 wt % when the ZnMOF-1 sample was first ground to a powder and then stirred in water (Supplementary Table 1, Supplementary Fig. 16). Single crystals of ZnMOF-1 measured roughly from 5 μm to hundreds of μm in length; in comparison, most crystals of ground ZnMOF-1 were found to be smaller than 0.5 μm (Supplementary Fig. 16). The increased formation of ZnMOF-inter when agitation and smaller sample crystallite sizes were employed is indicative of increased exchange between guest DMF and solvent water. The consistency in data between cryo-EM and XRD methods also confirms that the dried crystals of ZnMOF-1 used for SCXRD and PXRD experiments retain the same structure as the crystals frozen in the hydrated state for cryo-EM.

Multinuclear solid state NMR studies

¹³C CP/MAS and ¹H MAS SSNMR: The various intermediate states are products that appear to be strongly linked to the duration of water exposure. However, the origins of both distinct reaction pathways remain unclear. Multinuclear SSNMR spectroscopy was employed to monitor the local structure around the linkers and the Zn local environment during the structural evolution. ¹³C CP/MAS and ¹H MAS SSNMR spectra of ZnMOF-1 samples treated in water are illustrated in Fig. 5. All ¹³C and ¹H NMR resonances in the as-made ZnMOF-1 spectra arise from the BTEC and Trz linkers, along with guest DMF molecules (Fig. 5).

The ¹³C NMR signals are significantly altered after stirring ZnMOF-1 in water for just 30 seconds (*i.e.*, ZnMOF-1-30s). Resonances are generally broadened and some are split. The C5 carboxylate resonance fragments into a major signal along with several minor signals ranging from 170 to 178 ppm, which indicates new bonds have been formed between Zn and carboxylate oxygen atoms (C1) of the free BTEC carboxylate groups; the ¹³C chemical shifts of these new signals are similar to those of the ZnMOF-2 carboxylate atoms. ¹³C and ¹H SSNMR spectra continued to evolve with increasing stirring time. For example, in the Zn-O bound C5 carboxylate region, the number of ¹³C resonances increased from one in pure ZnMOF-1 to four in ZnMOF-1-30min, decreased to three in ZnMOF-1-4h, and then became two well-defined signals in the spectrum of ZnMOF-1-24h. Other trends of gradual spectral evolution can also be observed in other ¹³C resonances as well as the H6, H2, and H3 ¹H linker resonances (Fig. 5). The multiple changes in ¹H and ¹³C SSNMR spectra linked to duration of water exposure supports our hypothesis of ZnMOF-1 structural evolution to ZnMOF-4 and ZnMOF-inter through multiple intermediate materials.

There are several other features in the ¹H SSNMR spectra indicative of ZnMOF structural features and evolution. Two new ¹H signals between 12 and 15 ppm appear in the ¹H SSNMR spectrum of ZnMOF-1-15min, which are assigned to H₂O molecules coordinated to the Zn centers (Fig. 5b, Supplementary Fig. 17)⁶⁰. There is also a low intensity ¹H signal at 2.6 ppm in the spectrum of ZnMOF-1-24h (Fig. 5b, inset, bottom right), which is assigned to a small amount of water adsorbed in the pores of ZnMOF-4. The ¹H MAS spectrum of ZnMOF-1-30s also

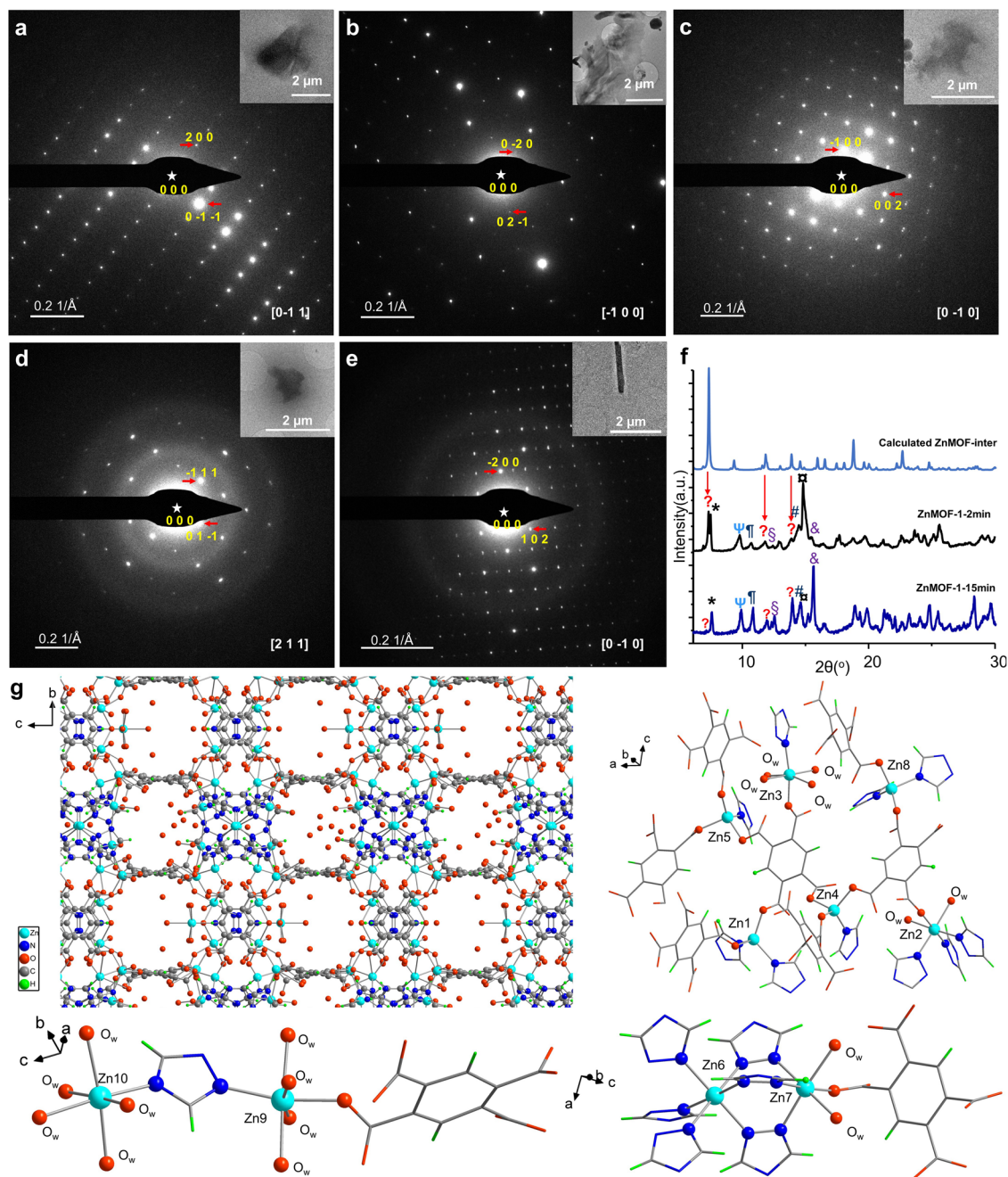


Fig. 4 | Cryo-EM images of Zn MOFs along with the crystal structure of ZnMOF-inter. The electron diffraction patterns of **a** ZnMOF-1, **b** ZnMOF-2, **c** ZnMOF-3, **d** ZnMOF-4 and **e** ZnMOF-inter crystals. The corresponding TEM images are shown as insets. A comparison between the calculated PXRD patterns of ZnMOF-inter and

water treated ZnMOF-1 samples is given in **f**, using the symbols defined in Fig. 3. The crystal structure of ZnMOF-inter, along with the ten Zn sites, are depicted in **g**. The pores are filled with water in ZnMOF-inter, and the O_w label denotes the oxygen atoms of coordinated water.

has an emerging resonance at 4.7 ppm, which is assigned to the methyl hydrogen of coordinated DMF in ZnMOF-2 and denoted H5'. The intensity of the H5' ^1H resonance increases with water exposure time, reaches a maximum in the spectrum of ZnMOF-1-2min, and is not visible after 1 h, confirming that the coordinated DMF species are only associated with the unstable ZnMOF-2 intermediate state. In contrast, uncoordinated guest DMF persists within the pores for an extended time, indicating that diffusion of DMF molecules from ZnMOF-1 into the surrounding water is a slow process.

^1H and ^{13}C SSNMR results show that guest DMF remains in ZnMOF-1 at least 1 h after water immersion, which is likely due to DMF (i) hydrogen bonding with the MOF and (ii) partially blocking the pores,

where both factors prevent water from quickly entering the framework. The extended residence of DMF also explains why there are no water molecules in the structure of ZnMOF-3. The SSNMR results support our hypothesis of both structural transformation pathways in ZnMOF-1 being associated with DMF diffusion. Fast exchange between DMF with water on the surface of crystals or within small crystallites leads to the formation of ZnMOF-inter, and sends the material on the pathway to dissolution. A slow diffusion of water into single crystals and larger crystallites affords sufficient time for the material to evolve through several intermediates and eventually produce ZnMOF-4. In an alternate situation where a significant amount of water could rapidly enter all pores of ZnMOF-1, ZnMOF-1 would likely proceed to ZnMOF-

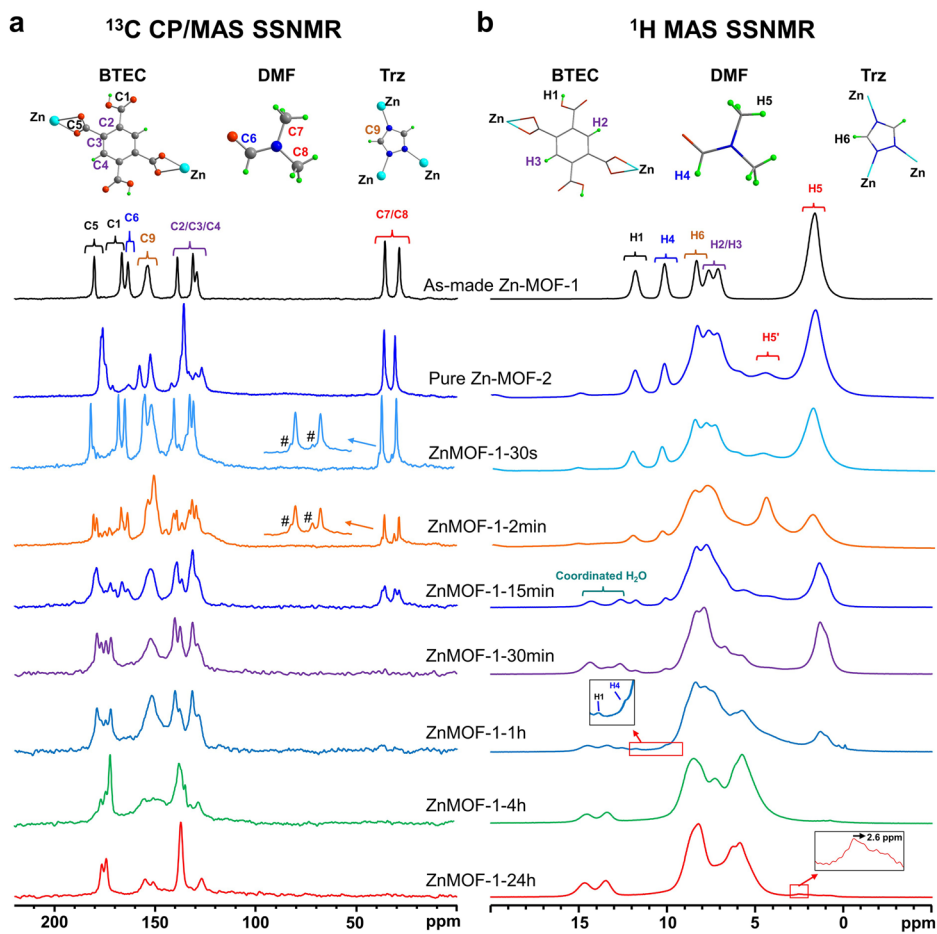


Fig. 5 | SSNMR spectra of Zn MOFs samples at different conditions. The **a** ^{13}C CP/MAS and **b** ^1H MAS SSNMR spectra of as made ZnMOF-1, pure ZnMOF-2, and water-treated ZnMOF-1 samples are shown. The pound symbol (#) denotes resonances assigned to C7 and C8, which are assigned to coordinated DMF within ZnMOF-2.

The H5' label marks signals from the methyl hydrogen atoms of coordinated DMF in ZnMOF-2. The low intensity ^1H signal at 2.6 ppm in the spectrum of ZnMOF-1-24h is assigned to a small amount of water adsorbed in the pores of ZnMOF-4.

inter and then quickly dissolve, preventing the formation of any significant amount of ZnMOF-4.

^{67}Zn SSNMR spectroscopy: Natural abundance ^{67}Zn static SSNMR experiments were carried out at high magnetic fields of 19.6 and 21.1 T to directly probe the Zn local environments during the water-induced structural transformation of ZnMOF-1 (Supplementary Fig. 18a). Plane-wave DFT calculations of the ^{67}Zn NMR parameters in ZnMOF-1/2/3/4 were also performed in order to help assign experimental resonances to specific species (Supplementary Fig. 18b). These ^{67}Zn SSNMR experimental results also clearly support our model of two structural evolution pathways; a detailed discussion of ^{67}Zn SSNMR results can be found in the SI.

AIMD and GCMC calculations

Calculations were performed to evaluate the MOF hydrolytic stability at a molecular level. The structure of as-made ZnMOF-1 with DMF guests was directly exposed to water molecules in *ab initio* molecular dynamics (AIMD) simulations. The results indicated that the as-made ZnMOF-1 structure is stable in the presence of concentrated water vapor (Supplementary Fig. 20), in agreement with PXRD data obtained from ZnMOF-1 samples exposed to high humidity environments (Fig. 1c); in contrast, as-made ZnMOF-1 is not stable upon immersion in liquid water. DMF guests are retained in the ZnMOF-1 structure during exposure to water vapor and do not diffuse out of the system, which prevents water molecules from forming an extended hydrogen bonding network within the pores, and increases the hydrolytic

stability of ZnMOF-1. The concentration of water molecules in humid environments is insufficient to trigger efficient solvent exchange of DMF for H_2O in ZnMOF-1, and the MOF accordingly remains intact after exposure to water vapor. In contrast, immersion in liquid water permits DMF guests to diffuse out of the MOF, which then makes ZnMOF-1 vulnerable to water attack and associated structural transformations.

To further investigate the hydrolytic stability of empty (*i.e.*, activated) ZnMOF-1 and ZnMOF-2, the guest DMF molecules in both structures were removed prior to grand canonical Monte Carlo (GCMC) simulations. The maximum water adsorption inside ZnMOF-1 and -2, along with those of ZnMOF-3, -4 and -inter, were determined (Fig. 6a). ZnMOF-1 and ZnMOF-2 were calculated to accommodate 32 water molecules⁶¹. The water adsorption capacities of ZnMOF-3 and ZnMOF-4 are limited by their narrower pores, leading to capacities of 10 and 12 water molecules, respectively. In contrast, up to 96 water molecules could be loaded into the unit cell of ZnMOF-inter due to its large pore and the extensive hydrogen bonding network among coordinated water.

The water-loaded ZnMOF-1, -2, -3 and -4 MOFs were subjected to AIMD simulations to evaluate their hydrolytic stability (Fig. 6b). The change in MOF unit cell volume after water exposure is a key indication of hydrolytic stability that is commonly used to evaluate MOF structural stability^{49,50}. The unit cell volumes of ZnMOF-1 and ZnMOF-2 drastically increases with greater numbers of guest water molecules, suggesting that these structures are not stable and will collapse. The

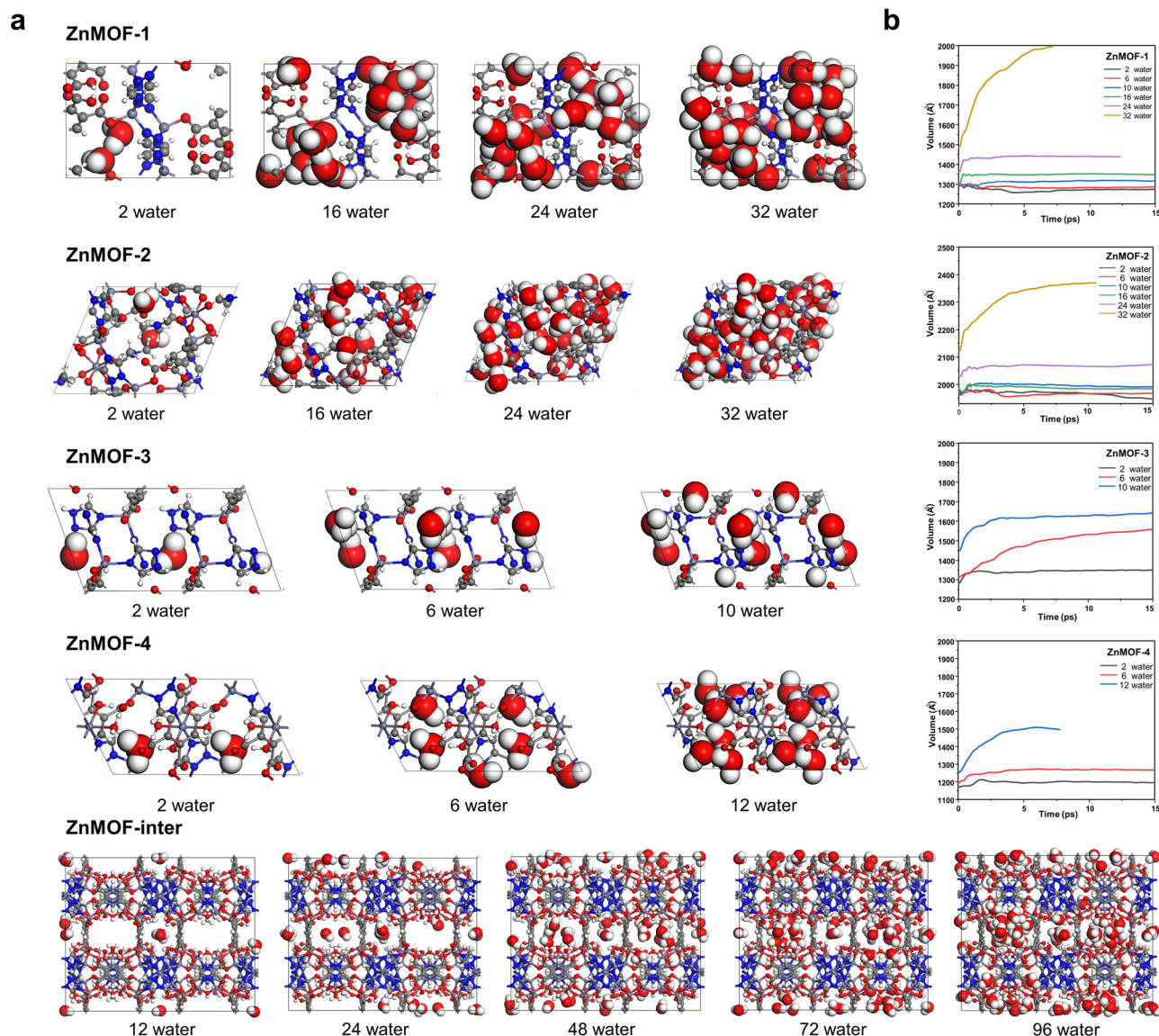


Fig. 6 | Theoretical calculation on Zn MOFs when exposed to water. **a** GCMC snapshots of ZnMOF-1/2/3/4-inter with adsorbed water molecules. **b** The simulated unit cell volume change of ZnMOF-1/2/3/4 loaded with different water molecules during a time period of 15 ps.

apparent vulnerability of empty ZnMOF-1 and -2 to structural collapse in water supports our hypothesis that the slow diffusion of DMF in as-made ZnMOF-1 prevents rapid water penetration into the framework, and again implicates DMF as the key reason for the formation of intermediate ZnMOF states. Calculations on ZnMOF-3 and ZnMOF-4 reveal increased structural stabilities after water adsorption, and their unit cell volumes are generally steady after ca. 5 ps (Fig. 6b). When comparing ZnMOF-3 and -4, calculations indicate that ZnMOF-4 is more structurally robust upon water immersion. At a loading level of six water molecules and a simulation time of 15 ps, the cell volume of ZnMOF-3 increased from ca. 1310 \AA^3 to 1550 \AA^3 (18% gain) but the cell volume of ZnMOF-4 was relatively unchanged from ca. 1200 \AA^3 to ca. 1250 \AA^3 (4% gain); the very small increase in ZnMOF-4 cell volume is suggestive of enhanced hydrolytic stability in this material versus ZnMOF-1, -2, and -3. The very large unit cell of ZnMOF-inter poses a computational challenge and prevents further study via AIMD simulations. However, the significant increase in unit cell volume from ZnMOF-2 (3774 \AA^3) to ZnMOF-inter (17881 \AA^3), paired with the rapid disappearance of PXRD reflections upon water exposure (Fig. 4f), agrees with the trend of MOF expansion and eventual collapse

indicated from the above calculations on ZnMOF-1 and ZnMOF-2. The removal of DMF from the pores of ZnMOF-1 and ZnMOF-2 before calculations adequately models the fast solvent exchange between exogenous water and incorporated DMF that leads to ZnMOF-inter. It again appears that both transformation pathways of ZnMOF-1 upon water immersion intimately rely on DMF diffusion rates.

Order of phase evolution in the two structural transformation pathways

At least five distinct MOF phases have been isolated and identified. While single crystals of ZnMOF-2, ZnMOF-3 and ZnMOF-4 appear in order after water immersion of ZnMOF-1, PXRD data indicates that ZnMOF-inter appears after ZnMOF-2, at approximately the same time as ZnMOF-3 and ZnMOF-4. It is not clear if ZnMOF-inter is formed from ZnMOF-1 or ZnMOF-2. In addition, after the dissolution of ZnMOF-inter, it is possible that the solvated Zn and linkers could then participate in the formation of ZnMOF-4.

To ascertain the identity of the direct precursor to ZnMOF-inter, pure powdered ZnMOF-2 was immersed in liquid water. The PXRD pattern of ZnMOF-2-1min confirms that ZnMOF-inter is derived

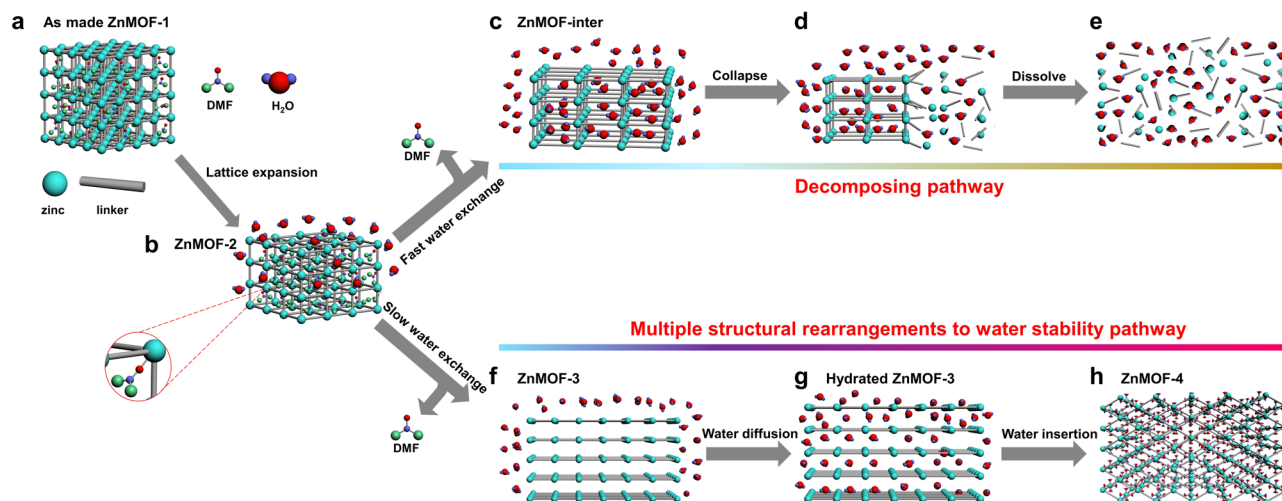


Fig. 7 | The proposed mechanism for the two structural transformation pathways in ZnMOF-1. As made ZnMOF-1 **a** first transforms into ZnMOF-2 **b** via lattice expansion. For the decomposition pathway, ZnMOF-2 first converts to ZnMOF-inter **c** via fast exchange between incorporated DMF and solvent water. ZnMOF-inter then collapses **d** and dissolves in water **e**; in the pathway to ZnMOF-4, DMF

molecules slowly diffuse out of the ZnMOF-2 framework, triggering a phase change to ZnMOF-3 in **f**, and then hydrated ZnMOF-3 **g**. The water molecules coordination with Zn centers in ZnMOF-3 leads to the formation of 3D ZnMOF-4 material that features octahedral Zn **h**.

directly from ZnMOF-2 (Supplementary Fig. 21). As there is no water in the structure of ZnMOF-3, and ZnMOF-inter contains both free and coordinated water, a structural transformation from ZnMOF-inter to ZnMOF-3 is highly unlikely. The ZnMOF-2-5min diffractogram verifies that ZnMOF-4 is formed directly from ZnMOF-3 (Supplementary Fig. 21). The possibility of dissolved ligands and Zn ions self-assembling in aqueous solution to form any of the documented crystalline phases was also examined. The filtrates from two samples, ZnMOF-1-15min and ZnMOF-1-24h, were isolated. Each filtrate was divided into two portions: one portion was allowed to evaporate in an open vial at room temperature and ambient conditions for one week, while the other portion was sealed in a 15 mL glass vial and placed in an oven heated to 100 °C for 3 d. Of the four resulting samples, only the ZnMOF-1-15min sample treated at 100 °C yielded a solid. A white powder weighing 1.1 mg was isolated; PXRD indicated the product was amorphous, with no traces of any crystalline materials (Supplementary Fig. 22). While this finding suggests that recrystallization of some phase from dissolved ligands and Zn ions is very unlikely, the possibility of this route influencing structural changes across both pathways cannot be completely excluded. The order of each structural change is now clear: ZnMOF-2 is formed from ZnMOF-1; a majority of the ZnMOF-2 crystals proceed to ZnMOF-3 and then ZnMOF-4, while a small portion of ZnMOF-2 changes into ZnMOF-inter and then dissolves in water.

Proposed mechanism

Detailed mechanisms for the two structural transformation pathways in ZnMOF-1 can now be proposed. As-made ZnMOF-1 (Fig. 7a) exhibits high stability in humid environments due to the presence of guest DMF molecules, which block the pores from H₂O penetration. When ZnMOF-1 is immersed in water it undergoes a lattice expansion. Due to the internal mobility of DMF guests along with the presence of free carboxyl linker groups proximate to Zn, new Zn-N and Zn-O bonds are formed and the ZnMOF-2 phase emerges (Fig. 7b). Two distinct structural changes may then occur to ZnMOF-2 depending on the degree of solvent penetration. In the decomposition pathway, the change from ZnMOF-2 to ZnMOF-inter occurs as water molecules rapidly replace guest and coordinated DMF, resulting in water bound to half of the zinc sites (Fig. 7c). ZnMOF-inter contains tetrahedral Zn sites that are vulnerable to solvent water attack, and the material eventually collapses (Fig. 7d) and dissolves in water (Fig. 7e). The

decomposition pathway is more probable in smaller crystallites and powders of ZnMOF-2, which permit faster exchange between incorporated DMF and solvent water molecules.

In ZnMOF-2 crystallites of moderate to large size, slow diffusion of internal DMF molecules out of the framework first leads to the formation of 1D chain-like ZnMOF-3 (Fig. 7f), which contains no water in its crystal structure. The chain structure allows water to freely diffuse between the layers and attack the tetrahedral Zn centers within ZnMOF-3 (Fig. 7g). The insertion of water molecules at Zn breaks the Zn-O^{carboxylate} bonds, forming a six coordinate Zn1 center with four coordinated water molecules in ZnMOF-4 (Fig. 7h). ZnMOF-4 has a high hydrolytic stability due to a combination of the stable Zn1 octahedral geometry along with the steric shielding and resulting chemical inertness of Zn2. While this work clearly demonstrates there are two distinct structural transformation pathways in which DMF solvent plays a key role, a complex equilibrium may additionally exist between different crystalline phases in the presence of water, with ZnMOF-4 being the most stable.

Discussion

Two routes of structural changes have been observed in a Zn MOF after exposure to liquid water. One pathway involves a rarely-documented series of multiple structural rearrangements that results in a water-stable Zn MOF with enhanced water sorption capacity, while the other route leads to an unstable intermediate MOF followed by decomposition. All prominent intermediate and final states have been characterized using a combination of advanced techniques including cryo-EM, microED, SCXRD, multinuclear SSNMR, and theoretical calculations.

This work unambiguously demonstrates that the diffusion rate of guest DMF solvent plays a critical role in determining which two structural transformation pathways occur. The fast exchange between solvent water and guest DMF leads to the decomposition route, while slow DMF diffusion from the framework leads to the formation of water-stable ZnMOF-4. Our findings present a unique example that demonstrates how water-sensitive MOFs may not necessarily lose crystallinity and porosity upon water exposure. Zinc-based MOFs with vulnerable tetrahedral Zn sites are able to self-heal after water exposure into a water-stable structure via slow solvent exchange. The identification of transient ZnMOF-inter by cryo-EM has shed further light on how MOFs may decompose in water. This discovery highlights how the type of

solvent used in MOF synthesis is a unique lever of control that is strongly connected to the resulting MOF stability and reactivity; carefully adjusting the crystallite size and incorporated solvent of water-sensitive MOFs can be an alternative route to synthesizing stable MOFs that are otherwise unattainable through conventional methods. We point out that small amounts of organic molecules and Zn species are also liberated during the reactions. Although they do not affect the conclusions presented, their behavior in solution does warrant future investigation. The experimental protocol detailed in this manuscript provides a foundation for other researchers seeking to elucidate complicated solvent-induced structural changes in MOFs. Investigating solvent-triggered structural evolution in other systems, especially if liquid or gas phases are involved, may necessitate the incorporation of several other techniques (e.g., liquid chromatography–mass spectrometry, gas chromatography–mass spectrometry, Raman spectroscopy, etc.).

Methods

Preparation of ZnMOF-1 (Zn(BTEC)(Trz))

As-made ZnMOF-1 was synthesized using the reported method³⁶ with some modifications, as described below. A mixture of 0.1487 g $\text{Zn}(\text{NO}_3)_2 \cdot 6\text{H}_2\text{O}$ (Sigma-Aldrich, 98%), 0.0697 g Trz (Sigma-Aldrich, 98%) and 0.1270 g BTEC (Alfa Aesar, 96%) was dissolved in 5.00 mL of DMF and magnetically stirred for 10 minutes, yielding a clear solution. The resulting mixture was then sealed in a 15 mL glass vial and placed in an oven maintained at 100 °C for 24 h. The resulting colorless crystals were isolated via vacuum filtration and washed with 10 mL of DMF three times.

SCXRD measurements

A Bruker Kappa Axis Apex2 diffractometer with the temperature maintained at 110 K was used for ZnMOF-1/3/4 data collection. For ZnMOF-2, a suitable single crystal was selected and collected at 110 K on a Bruker D8 VENTURE Metaljet PHOTON II diffractometer. The frame integration was performed using SAINT⁶². The resulting raw data was scaled and absorption corrected using multi-scan averaging of symmetry equivalent data in SADABS⁶³. Crystal structures were solved using the SHELXT program, with all non-hydrogen framework atomic positions obtained from the initial solution and hydrogen atoms introduced at idealized positions. The structure was then refined using SHELXL-2014⁶⁴.

Frozen sample preparation for cryo-EM

A powdered sample of ZnMOF-1 was dispersed in ultrapure water (99.999 %) and stirred at room temperature for a specific time. A 4.0 μL droplet of the stirred and dispersed MOF sample was then pipetted onto a freshly glow-discharged Quantifoil Au grid (Electron Microscopy Sciences). After ca. 30 s, the grids were blotted at 100 % humidity and plunge-frozen in liquid ethane using a Vitrobot Mark IV instrument (Thermo Fisher Scientific).

Cryo-EM diffraction data collection

The TEM images and diffraction data were collected on a FEI Talos F200C electron microscope equipped with a FEI Ceta camera. The grids were screened at low magnification to identify crystals that were well separated from other crystals. The diffraction patterns and tilt series of these crystals were collected using SerialEM (version 3.8)⁶⁵, employing a tilt angle from -48.8° to $+48.8^\circ$, a rotation rate of $0.5^\circ/\text{s}$, and an exposure rate below $0.05 \text{ e}/\text{\AA}^2/\text{s}$. Low dose settings were used throughout the screening and data collection.

¹³C SSNMR experiments at 9.4 T

All ¹³C cross-polarization/magic-angle spinning (CP/MAS) SSNMR experiments were carried out on a Varian InfinityPlus wide-bore NMR spectrometer equipped with a 4 mm HXY Varian/Chemagnetics probe, operating at a magnetic field strength of 9.4 T ($\nu_0(^{13}\text{C}) = 100.5 \text{ MHz}$). All experiments used a spinning frequency of 14 kHz, a CP contact time of

7 ms, a recycle delay of 2 s, and 1300 scans were collected. The ¹³C chemical shifts were referenced to tetramethylsilane (TMS) using the high frequency ¹³C resonance of adamantane as a secondary reference at 38.52 ppm⁶⁶.

¹H SSNMR experiments at 21.1 T

The ¹H MAS NMR spectra of ZnMOF-1 and related samples were acquired at 21.1 T ($\nu_0(^1\text{H}) = 899.4 \text{ MHz}$) using a Bruker Avance II spectrometer and a Bruker 2.5-mm HX MAS probe. A spinning frequency of 31.25 kHz and a recycle delay of 32 s were used, with 32 scans collected for each experiment. Adamantane was used as a secondary ¹H chemical shift reference at 1.85 ppm⁶⁶.

⁶⁷Zn SSNMR experiments at 19.6 and 21.1 T

The static ⁶⁷Zn NMR spectra of as-made ZnMOF-1, ZnMOF-1-15min, and ZnMOF-1-24h were collected at 21.1 T using a home-built 7-mm single-channel static probe, a Bruker Avance II console, and a 90°-90° quadrupolar echo pulse sequence. The ⁶⁷Zn static spectra of ZnMOF-2 and ZnMOF-1-30s were acquired at 19.6 T using a 5 mm home-built single-channel static probe, a Bruker Avance NEO console, and a 90° - 90° spin-echo pulse sequence. All ⁶⁷Zn chemical shifts were referenced to 1.0 M $\text{Zn}(\text{NO}_3)_2$ ($\delta_{\text{iso}} = 0.0 \text{ ppm}$)⁶⁷. The number of scans acquired was 64,000 for the spectrum of as-made ZnMOF-1, 3,735,552 for ZnMOF-2, 1,225,728 for ZnMOF-1-30s, 320,000 for ZnMOF-1-15min and 360,000 for ZnMOF-1-24h. The 90° pulse lengths employed were 3.0 μs and 2.5 μs for samples collected at 21.1 T and 19.6 T, respectively. A pulse delay of 0.25 s was used to acquire the spectra of as-made ZnMOF-1, ZnMOF-1-15min, and ZnMOF-1-24h. For ZnMOF-2 and ZnMOF-1-30s, the pulse delay utilized was 0.10 s.

TGA, IR spectroscopy and TEM

Thermogravimetric analysis (TGA) measurements were performed using a Beijing Henvin Scientific Instrument Factory HQT-3 instrument. All samples were heated from room temperature to 1000 °C at a rate of 10 °C/min under N₂ flow. The TGA data of ZnMOF-1, ZnMOF-2, and ZnMOF-4 is given in Supplementary Fig. 23. Infrared (IR) experiments were collected using a Thermo Nicolet NEXUS-870 instrument. The IR spectra of ZnMOF-1, ZnMOF-2, and ZnMOF-4 are shown in Supplementary Fig. 24. Transmission electron microscopy (TEM) images were performed with a FEI Tecnai F30.

Powder X-ray diffraction (PXRD) experiments, density functional theory (DFT) calculations, microED and grand canonical Monte Carlo (GCMC) calculations

All details can be found in the supporting information.

Data availability

The crystallographic data for this paper were deposited under Cambridge Crystallographic Data Centre (CCDC) numbers 2008248, 2008249, 2008250, 2226458 and 2284361 which can be obtained by visiting the CCDC web site (www.ccdc.cam.ac.uk/data_request/cif). Source data are provided with this paper.

References

1. Della Rocca, J., Liu, D. & Lin, W. Nanoscale metal–organic frameworks for biomedical imaging and drug delivery. *Acc. Chem. Res.* **44**, 957–968 (2011).
2. Kitagawa, S. Metal–organic frameworks (MOFs). *Chem. Soc. Rev.* **43**, 5415–5418 (2014).
3. Furukawa, H., Cordova, K. E., O’Keeffe, M. & Yaghi, O. M. The chemistry and applications of metal–organic frameworks. *Science* **341**, 1230444 (2013).
4. Jiang, J., Furukawa, H., Zhang, Y.-B. & Yaghi, O. M. High methane storage working capacity in metal–organic frameworks with acrylate links. *J. Am. Chem. Soc.* **138**, 10244–10251 (2016).

5. Peng, Y. L. et al. Robust ultramicroporous metal–organic frameworks with benchmark affinity for acetylene. *Angew. Chem. Int. Ed.* **57**, 10971–10975 (2018).
6. Kreno, L. E. et al. Metal–organic framework materials as chemical sensors. *Chem. Rev.* **112**, 1105–1125 (2012).
7. Hu, Z., Deibert, B. J. & Li, J. Luminescent metal–organic frameworks for chemical sensing and explosive detection. *Chem. Soc. Rev.* **43**, 5815–5840 (2014).
8. Dhakshinamoorthy, A. & Garcia, H. Catalysis by metal nanoparticles embedded on metal–organic frameworks. *Chem. Soc. Rev.* **41**, 5262–5284 (2012).
9. Huang, Y.-B., Liang, J., Wang, X.-S. & Cao, R. Multifunctional metal–organic framework catalysts: synergistic catalysis and tandem reactions. *Chem. Soc. Rev.* **46**, 126–157 (2017).
10. Kondo, Y., Kuwahara, Y., Mori, K. & Yamashita, H. Design of metal–organic framework catalysts for photocatalytic hydrogen peroxide production. *Chem.* **8**, 2924–2938 (2022).
11. Chang, Z. Recent progress in host–guest metal–organic frameworks: Construction and emergent properties. *Coord. Chem. Rev.* **476**, 214921 (2023).
12. Xiao, Y., Li, S., Xu, J. & Deng, F. Solid-state NMR studies of host–guest chemistry in metal–organic frameworks. *Curr. Opin. Colloid Interface Sci.* **61**, 101633 (2022).
13. Chen, S. et al. Cleaving carboxyls: Understanding thermally triggered hierarchical pores in the metal–organic framework MIL-121. *J. Am. Chem. Soc.* **141**, 14257–14271 (2019).
14. Howarth, A. J. et al. Chemical, thermal and mechanical stabilities of metal–organic frameworks. *Nat. Rev. Mater.* **1**, 15018 (2016).
15. Burtch, N. C., Jasuja, H. & Walton, K. S. Water stability and adsorption in metal–organic frameworks. *Chem. Rev.* **114**, 10575–10612 (2014).
16. Bai, Y. et al. Zr-based metal–organic frameworks: design, synthesis, structure, and applications. *Chem. Soc. Rev.* **45**, 2327–2367 (2016).
17. Fan, W. et al. Aluminum metal–organic frameworks: from structures to applications. *Coord. Chem. Rev.* **489**, 215175 (2023).
18. Park, K. S. et al. Exceptional chemical and thermal stability of zeolitic imidazolate frameworks. *Proc. Natl Acad. Sci.* **103**, 10186–10191 (2006).
19. He, T., Kong, X.-J. & Li, J.-R. Chemically stable metal–organic frameworks: rational construction and application expansion. *Acc. Chem. Res.* **54**, 3083–3094 (2021).
20. Lin, J.-B. et al. A scalable metal–organic framework as a durable physisorbent for carbon dioxide capture. *Science* **374**, 1464–1469 (2021).
21. Ryu, U. et al. Recent advances in process engineering and upcoming applications of metal–organic frameworks. *Coord. Chem. Rev.* **426**, 213544 (2021).
22. Silva, P., Vilela, S. M., Tome, J. P. & Paz, F. A. A. Multifunctional metal–organic frameworks: from academia to industrial applications. *Chem. Soc. Rev.* **44**, 6774–6803 (2015).
23. Hanikel, N., Prévot, M. S. & Yaghi, O. M. MOF water harvesters. *Nat. Nanotechnol.* **15**, 348–355 (2020).
24. Kim, H. et al. Water harvesting from air with metal–organic frameworks powered by natural sunlight. *Science* **356**, 430–434 (2017).
25. Mouchaham, G. et al. Metal–organic frameworks and Water: From old enemies to friends? *Trends Chem.* **2**, 990–1003 (2020).
26. Wang, S. et al. A robust large-pore zirconium carboxylate metal–organic framework for energy-efficient water-sorption-driven refrigeration. *Nat. Energy* **3**, 985–993 (2018).
27. Kaye, S. S., Dailly, A., Yaghi, O. M. & Long, J. R. Impact of preparation and handling on the hydrogen storage properties of Zn₄O(1, 4-benzenedicarboxylate)₃(MOF-5). *J. Am. Chem. Soc.* **129**, 14176–14177 (2007).
28. Guo, P., Dutta, D., Wong-Foy, A. G., Gidley, D. W. & Matzger, A. J. Water sensitivity in Zn₄O-based MOFs is structure and history dependent. *J. Am. Chem. Soc.* **137**, 2651–2657 (2015).
29. Al-Janabi, N. et al. Mapping the Cu-BTC metal–organic framework (HKUST-1) stability envelope in the presence of water vapour for CO₂ adsorption from flue gases. *Chem. Eng. J.* **281**, 669–677 (2015).
30. Yang, H. et al. Ultrastable high-connected chromium metal–organic frameworks. *J. Am. Chem. Soc.* **143**, 14470–14474 (2021).
31. Ding, M., Cai, X. & Jiang, H.-L. Improving MOF stability: approaches and applications. *Chem. Sci.* **10**, 10209–10230 (2019).
32. Chiong, J. A. et al. An exceptionally stable metal–organic framework constructed from chelate-based metal–organic polyhedra. *J. Am. Chem. Soc.* **142**, 6907–6912 (2020).
33. Burtch, N. C. et al. In situ visualization of loading-dependent water effects in a stable metal–organic framework. *Nat. Chem.* **12**, 186–192 (2020).
34. Dong, Q. et al. Confining water nanotubes in a Cu₁₀O₁₃-based metal–organic framework for propylene/propane separation with record-high selectivity. *J. Am. Chem. Soc.* **145**, 8043–8051 (2023).
35. Wang, R., Shi, K., Liu, J., Snurr, R. Q. & Hupp, J. T. Water-accelerated transport: vapor-phase nerve agent simulant delivery within a catalytic zirconium metal–organic framework as a function of relative humidity. *J. Am. Chem. Soc.* **145**, 13979–13988 (2023).
36. Meng, X. et al. A stable, pillar-layer metal–organic framework containing uncoordinated carboxyl groups for separation of transition metal ions. *Chem. Commun.* **50**, 6406–6408 (2014).
37. Luo, X.-L., Yin, Z., Zeng, M.-H. & Kurmoo, M. The construction, structures, and functions of pillared layer metal–organic frameworks. *Inorg. Chem. Front.* **3**, 1208–1226 (2016).
38. Mukherjee, S. et al. Ultramicropore engineering by dehydration to enable molecular sieving of H₂ by calcium trimesate. *Angew. Chem. Int. Ed.* **59**, 16188–16194 (2020).
39. Mehio, N., Dai, S. & Jiang, D. Quantum mechanical basis for kinetic diameters of small gaseous molecules. *J. Phys. Chem. A* **118**, 1150–1154 (2014).
40. Wang, X.-S. et al. Three-dimensional porous metal–metalloporphyrin framework consisting of nanoscopic polyhedral cages. *J. Am. Chem. Soc.* **133**, 16322–16325 (2011).
41. Kalmutzki, M. J., Diercks, C. S. & Yaghi, O. M. Metal–organic frameworks for water harvesting from air. *Adv. Mater.* **30**, 1704304 (2018).
42. Jasuja, H., Burtch, N. C., Huang, Y.-g, Cai, Y. & Walton, K. S. Kinetic water stability of an isostructural family of zinc-based pillared metal–organic frameworks. *Langmuir* **29**, 633–642 (2013).
43. Brozek, C. K. et al. Dynamic DMF binding in MOF-5 enables the formation of metastable cobalt-substituted MOF-5 analogues. *ACS Cent. Sci.* **1**, 252–260 (2015).
44. Ghosh, S. K., Zhang, J. P. & Kitagawa, S. Reversible topochemical transformation of a soft crystal of a coordination polymer. *Angew. Chem. Int. Ed.* **46**, 7965–7968 (2007).
45. Zhang, J.-P., Liao, P.-Q., Zhou, H.-L., Lin, R.-B. & Chen, X.-M. Single-crystal X-ray diffraction studies on structural transformations of porous coordination polymers. *Chem. Soc. Rev.* **43**, 5789–5814 (2014).
46. Choi, S. B. et al. Reversible interpenetration in a metal–organic framework triggered by ligand removal and addition. *Angew. Chem.* **124**, 8921–8925 (2012).
47. Lo, S.-H. et al. Rapid desolvation-triggered domino lattice rearrangement in a metal–organic framework. *Nat. Chem.* **12**, 90–97 (2020).
48. Chowdhuri, D. S., Rana, A., Bera, M., Zangrando, E. & Dalai, S. 3D zinc (II) coordination polymers built up by triazole and benzene-polycarboxylate anions: Synthesis, crystal structure, thermal and photoluminescence characterization. *Polyhedron* **28**, 2131–2136 (2009).
49. Greathouse, J. A. & Allendorf, M. D. The interaction of water with MOF-5 simulated by molecular dynamics. *J. Am. Chem. Soc.* **128**, 10678–10679 (2006).
50. Han, S. S., Choi, S.-H. & Van Duin, A. C. Molecular dynamics simulations of stability of metal–organic frameworks against H₂O using

- the ReaxFF reactive force field. *Chem. Commun.* **46**, 5713–5715 (2010).
51. Taylor, J. M., Vaidyanathan, R., Iremonger, S. S. & Shimizu, G. K. H. Enhancing water stability of metal–organic frameworks via phosphate monoester linkers. *J. Am. Chem. Soc.* **134**, 14338–14340 (2012).
 52. Liu, X. et al. Three-step nucleation of metal–organic framework nanocrystals. *Proc. Natl Acad. Sci. USA.* **118**, e2008880118 (2021).
 53. Peng, X. et al. Observation of formation and local structures of metal–organic layers via complementary electron microscopy techniques. *Nat. Commun.* **13**, 1–9 (2022).
 54. Li, Y., Huang, W., Li, Y., Chiu, W. & Cui, Y. Opportunities for cryogenic electron microscopy in materials science and nanoscience. *ACS nano* **14**, 9263–9276 (2020).
 55. Li, Y. et al. Cryo-EM structures of atomic surfaces and host-guest chemistry in metal–organic frameworks. *Matter* **1**, 428–438 (2019).
 56. Meng, Z. et al. Unraveling the electrical and magnetic properties of layered conductive metal–organic framework with atomic precision. *Angew. Chem.* **134**, e202113569 (2022).
 57. Huang, Z. et al. Can 3D electron diffraction provide accurate atomic structures of metal–organic frameworks? *Faraday Discuss* **225**, 118–132 (2021).
 58. Low, J. J. et al. Virtual high throughput screening confirmed experimentally: porous coordination polymer hydration. *J. Am. Chem. Soc.* **131**, 15834–15842 (2009).
 59. Bellarosa, L., Calero, S. & López, N. Early stages in the degradation of metal–organic frameworks in liquid water from first-principles molecular dynamics. *PCCP* **14**, 7240–7245 (2012).
 60. Trickett, C. A. et al. Identification of the strong Brønsted acid site in a metal–organic framework solid acid catalyst. *Nat. Chem.* **11**, 170–176 (2019).
 61. Hanikel, N. et al. Evolution of water structures in metal–organic frameworks for improved atmospheric water harvesting. *Science* **374**, 454–459 (2021).
 62. Anonymous (Bruker-AXS, SAINT version 2013.8, 2013, Bruker-AXS, Madison, WI 53711, USA).
 63. Anonymous (Bruker-AXS, SADABS version 2012.1, 2012, Bruker-AXS, Madison, WI 53711 USA).
 64. Sheldrick, G. A short history of SHELX. *Acta Cryst.* **64**, 112–122 (2008).
 65. Mastronarde, D. N. Automated electron microscope tomography using robust prediction of specimen movements. *J. Struct. Biol.* **152**, 36–51 (2005).
 66. Hayashi, S. & Hayamizu, K. Chemical shift standards in high-resolution solid-state NMR (^{13}C , ^{29}Si , and ^1H nuclei). *Bull. Chem. Soc. Jpn.* **64**, 685–687 (1991).
 67. Harris, R. K., Becker, E. D., De Menezes, S. M. C., Goodfellow, R. & Granger, P. NMR nomenclature. Nuclear spin properties and conventions for chemical shifts (IUPAC Recommendations 2001). *Pure Appl. Chem.* **73**, 1795–1818 (2001).

Acknowledgements

S.C. and D.L. acknowledge financial support from the National Natural Science Foundation of China (no. 22105091 and no. 32171300) and Fundamental Research Funds for the Central Universities (lzujbky-2021-sp26 and lzujbky-2021-ct05). D.L. acknowledges the Supercomputing Center of Lanzhou University for providing computational resources. Y.H. thanks the Natural Sciences and Engineering Research Council of Canada for a Discovery Grant. A.Z. thanks the Natural Science

Foundation of Wuhan (2024040701010058). Access to the 21.1 T NMR spectrometer was provided by the Canadian National Ultrahigh-Field NMR Facility for Solids (Ottawa, Canada), a national research facility funded by a consortium of Canadian Universities, and managed by the National Research Council Canada. A portion of this work was performed at the National High Magnetic Field Laboratory in Florida, USA, which is supported by the National Science Foundation (NSF) DMR-2128556 and the State of Florida.

Author contributions

S.C., D.L., and Y.H. designed the project and experiments. S.C., M.C., and H.Z. prepared the samples and collected SCXRD, PXRD, and gas sorption data. S.C., B.E.G.L., I.H., and Z.G. collected and processed NMR data, and W.Z. conducted DFT calculations. W.C. and A.Z. did the GCMC and AIMD simulations. Z.Z. and D.L. performed cryo-EM and microED experiments. S.C. wrote the first draft of the manuscript and B.E.G.L. performed manuscript edits and revisions. All authors contributed to the interpretation of experimental results and final manuscript revisions.

Competing interests

The authors declare no competing interests.

Additional information

Supplementary information The online version contains supplementary material available at <https://doi.org/10.1038/s41467-024-54493-7>.

Correspondence and requests for materials should be addressed to Shoushun Chen, Dongsheng Lei or Yining Huang.

Peer review information *Nature Communications* thanks Jingui Duan, Wuzong Zhou and the other, anonymous, reviewer(s) for their contribution to the peer review of this work. A peer review file is available.

Reprints and permissions information is available at <http://www.nature.com/reprints>

Publisher's note Springer Nature remains neutral with regard to jurisdictional claims in published maps and institutional affiliations.

Open Access This article is licensed under a Creative Commons Attribution-NonCommercial-NoDerivatives 4.0 International License, which permits any non-commercial use, sharing, distribution and reproduction in any medium or format, as long as you give appropriate credit to the original author(s) and the source, provide a link to the Creative Commons licence, and indicate if you modified the licensed material. You do not have permission under this licence to share adapted material derived from this article or parts of it. The images or other third party material in this article are included in the article's Creative Commons licence, unless indicated otherwise in a credit line to the material. If material is not included in the article's Creative Commons licence and your intended use is not permitted by statutory regulation or exceeds the permitted use, you will need to obtain permission directly from the copyright holder. To view a copy of this licence, visit <http://creativecommons.org/licenses/by-nc-nd/4.0/>.

© The Author(s) 2024